Coupling mechanism of kinetic and thermal impacts of Rayleigh surface acoustic waves on the microdroplet.

Mubbashar Mehmood[1]*, Tariq Nawaz Chaudhary[1,2], Stephen Burnside[1], Umar F Khan[3], Richard Yongqing Fu[4], Baixin Chen[1]

[1]School of Engineering and Physical Sciences, Heriot-Watt University, Edinburgh, EH14 4AS, UK.

[2]Department of Mechanical Engineering, University of Engineering and Technology, Lahore, Pakistan.

[3]School of Engineering, Robert Gordon University, Garthdee Road, Aberdeen, AB10 7QB, UK.

[4]Faculty of Engineering and Environment, Northumbria University, Newcastle upon Tyne, NE1 8ST, UK.

*Corresponding author: Dr Mubbashar Mehmood, m.mehmood@hw.ac.uk

Abstract:

An experimental study has been conducted to investigate the coupling mechanism between thermal and kinetic impacts of surface acoustic waves (SAW) using a water droplet (25 µl) on the zinc oxide (*ZnO*) thin-film piezoelectric substrate fabricated on an aluminium plate. The temperature is measured by an infrared (*IR*) thermal camera, and fluid streaming was detected by particles image velocimetry (*PIV*). The input power ranges from 0.096 W to 3.2 W resulting in a temperature rise and streaming velocity in the droplet up to 55 °C and 24.6 mm/s, respectively. It is found that the thermal impact is insignificant at lower input power (<0.50 W); however, this becomes dominant when the input power is greater than 2.0 W. The study also found that heat inside the droplet is distributed via streaming from the heat source. The heat is distributed from the heat source where *SAW* power penetrates to the droplet. Another key finding of this investigation revealed that when the input power is greater than 0.50 W, inverse heat transfer from the droplet to the substrate is observed due to the increase in fluid temperatures.

Keywords: Rayleigh *SAW*, radiated heat transfer, energy absorbed, *ZnO* thin film

1. Introduction:

Microdroplets can be applied as a distinct biological reactor for research to achieve mixing, bio-reaction, heating etc., without diffusion through the droplet interface [1]. One kind of such reactor is the surface acoustic wave device, which is simple in principle and convenient in laboratory operations. When a radio frequency (*RF*) power is applied to the interdigital transducer (*IDT*) on a piezoelectric substrate, surface acoustic waves (*SAW)* generates [2]. By placing the droplet on the path where waves propagate, wave energy dissipates inside the droplet to cause not only internal streaming inside the droplet [3]–[5] but also the rise in temperature of the droplet [6]. The transfer of *SAW* energy into the droplet is due to the mismatch of the sound velocities in the liquid and solid substrate, the *SAW* energy (power) transferred to the droplet can be converted into kinetic and thermal energies. Kinetic energy generates the internal flow of fluid (streaming) [5], called kinetic impact in this study, whereas thermal energy heats the droplet and the substrate [7], the thermal impact. Both kinetic and thermal impacts will be boosted with the increase in *SAW* input power/voltage [8],[9].

Regarding the thermal impacts, an experimental study conducted using 128° lithium niobate ($LiNbO_3$) and ST X quartz (direction cut) substrate reported that heating of the droplet is mainly caused by acoustic streaming in the droplet [7]. Meanwhile, another study found that heating of the droplet is primarily due to the longitudinal waves [6]. It was reported that along with the acoustic field, an electric field is also applied to the *IDTs* that heats the substrate and enhance streaming by 2-3 times in certain situations [10]. Therefore, the rise in temperature of the droplet is a combination of the heat interactions of electric field thermal effect (Joule heat) on the substrate and acousto-thermal effect by acoustic waves [11]. From experimental studies, it has been found that the temperature of the droplet (T_d) is higher near the *SAW* entry than the temperature on the other side of the droplet, which is considered as the result of the radiation heat by acoustic waves [12], while no details on the temperature distribution were reported. *SAW* causes good mixing inside the liquid as well as an increase in the liquid temperature. Some living organisms lose their properties at high temperatures (between 50 and 60 °C), but this can be overcome by using a thermostable enzyme. An increase in temperature becomes a means to enhance the enzyme reaction that can help to manufacture a highly sensitive biosensor. *SAW* can enhance mixing which boosts electrochemical reaction characteristics of low molecular weight [8]. Metal-organic frameworks (*MOF*s) are a class of coordination polymers constructed from cluster nodes and functional organic ligands through coordination bonds [14]. They have been used in drug delivery, sensing, detection and biomedical applications [15]. Most *MOF*s have nanopores that hinder the diffusion of bulky guest molecules and limit their interactions with active sites within the *MOF* structure. Hierarchically porous (*HP*) *MOF*s can overcome this issue. Methods used to generate *HP* within *MOF* takes time and high temperatures. *SAW* assist in the crystallisation technology which synthesizes *MOF*s efficiently within 4 mins [16]. Moreover, the thermal impact caused by the standing surface acoustic waves (*SSAW*) increases the droplet temperature which reduces the crystallisation period [8].

Some biological applications require a constant temperature of 37 °C to keep cells alive [17]; however, some of them, for example, polymerase chain reaction *(PCR)*, require homogeneous controlled heating (94-96 °C) and cooling (50-65 °C) cycles [18]. A *SAW*-based temperature control system has been developed by changing the duty factor or changing the applied input signal voltage/power and using the $LiNbO_3$ as a substrate [6], [19]. Recently, a comparison of acoustothermal heating characteristics of thin-film *SAW* devices (*AlN/Si* and *ZnO/Si*) have been investigated to control the temperature of the droplet [20]. The study concludes that *AlN/Si* devices demonstrate superior heating characteristics over other thin-film *SAW* devices [20]. *AlN/Si* exhibit higher surface temperature and quicker response than *ZnO/Si* devices for the same input power [21].

A study of *SAW* atomisation revealed that temperature rise in the liquid is due to viscous dissipation of the irradiated longitudinal wave energy and not from the inelastic effects of the substrate [22]. The

heating effect for focused droplet nebulization was investigated and it has been found that varying the central angle of the *IDT* from 30º to 90º can lead to significantly higher temperatures in the centre due to higher focused wave energy [23]. Using 128° Y-cut X-propagating $LiNbO_3$ as a substrate, *SSAW* and channel-based system, it has been found that acoustothermal energy depends on the acoustic energy density and varies by changing the input power, frequency and size of the system. Numerical simulations show that heat generation is due to the conversion of pressure work to internal energy. Furthermore, hydrodynamic transportation of heat also causes a temperature rise of the liquid. Acoustic energy is a cause of potential energy and kinetic energy [8].

From the literature review, it was realized that various methods have been proposed to study the temperature rise of the droplet and streaming inside the droplet [6], [19], [20]. However, no one implemented mass, momentum and energy conservation principles and provided a clear understanding of the coupling mechanisms of 'heating' and 'streaming' caused by the *SAW* inside the droplet [6], [7], [12], [24]. By implementing these models, we can distinguish which part of the energy being penetrated inside the droplet enhances fluid mixing and temperature rise of the droplet.

Therefore, in this study, we comprehended the coupling mechanism and proposed a model to implement mass, momentum, and energy conservation principles. This paper has been divided into two main sections. The first section presents the proposed analysis model, followed by the methodology and design of the experiments. The second section includes results and discussion. As is well-known, bulk piezoelectric materials such as quartz and $LiNbO_3$ are difficult to integrate with silicon (*Si*)-based integrated circuits [25]. On the other hand, thin films, for example, *ZnO* has advantages such as low cost, reliability, high electromechanical coupling coefficient and the capability to integrate with *Si* process technology [26], [27]. Moreover, the $LiNbO_3$ wafer can be easily broken at high *SAW* powers due to the brittle nature of the material. However, cracking is rare in thin-film devices, even at a power value of 60-70 W [21]. On the other hand, AlN/Si *SAW* devices are good only for heating but are not good for actuation/kinetics inside the droplet [21]. *ZnO/Al* plate has a higher electromechanical coupling coefficient and larger Rayleigh angle which makes it better in terms of kinetics as well as in heating. Since this study is focused on the coupling of kinetic and heating of the droplet, therefore, *ZnO/Al* plate has been used in this study to investigate the kinetic and thermal impacts of *SAW* [21].

2. Methodology and Experimental Setup:

The schematic diagram of the experimental setup is shown in Figure 1. *ZnO* film with a thickness of ~5 µm was deposited on the aluminium (*Al*) plate of thickness 600 µm using a *DC* magnetron sputtering from *Zn* target at a *DC* power of 400 W and gases of Ar/O_2 (flow ratio of 10/15). Aluminum *IDT* electrodes were fabricated on the top of the *ZnO* film using conventional thermal evaporation and lift-off process. It consists of 50 finger pair of electrodes with an aperture of 10 mm. The resonant frequency

and signal amplitude of the *SAW* device was measured using a network analyzer (Agilent 8712ET). The 'resonant frequency' of the signal was found to be 26.300 MHz with a wavelength of 100 µm. Therefore, the calculated velocity of the waves on the aluminium *SAW* device in this study is 2630 m/s ($v=f\lambda$).

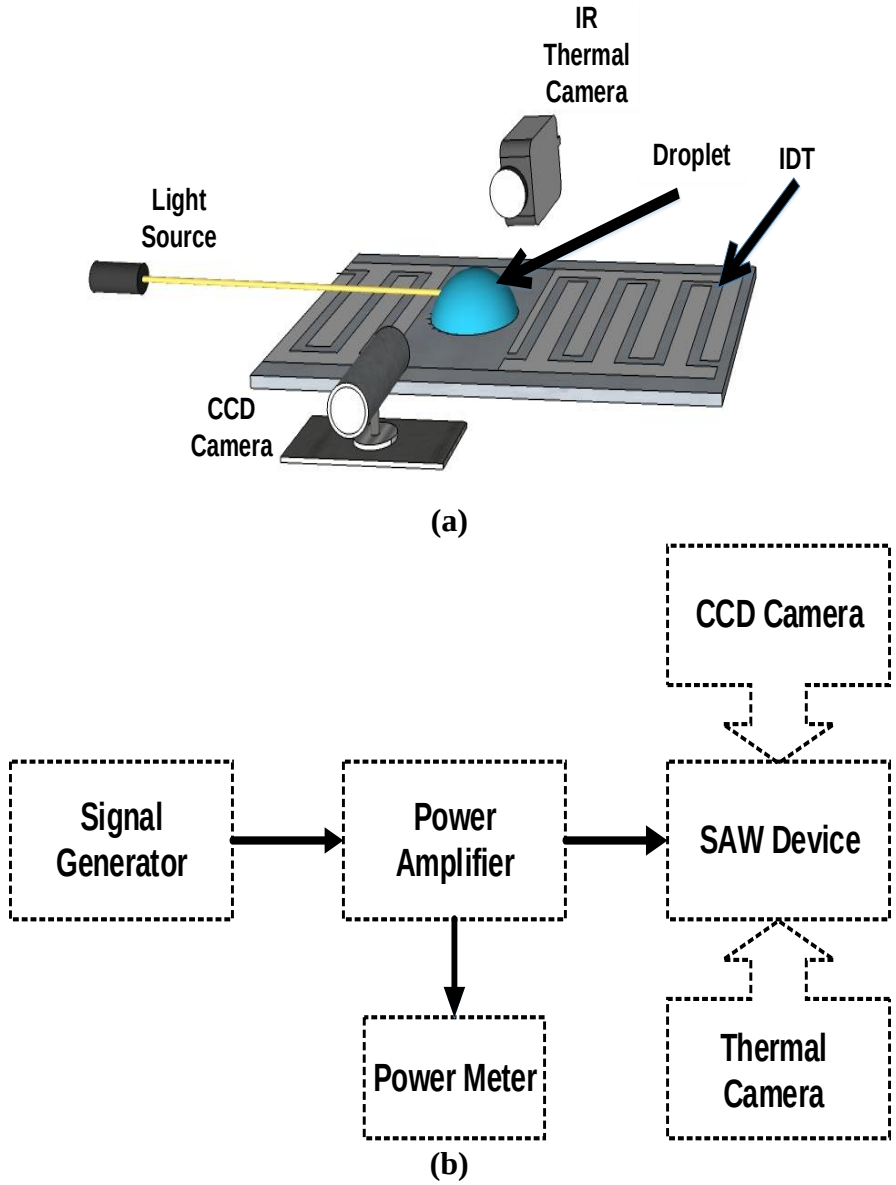

Figure 1: (a) Schematic diagram of experimental setup (b) Diagram of the *SAW* signal generation and data recording.

The *SAW* signal was generated using a radio frequency (*RF*) signal generator (Marconi Instruments 2024) at the resonant frequency and amplified using a power amplifier (Amplifier Research 75A250). A deionized (*DI*) water droplet of 25 µl was placed ~2 mm in front of the *IDT*. An RF power meter (Racal 9104) was used to measure the *RF* power input applied to the *IDT*. The device surface was coated with 200 nm thick CY-TOP (Asahi Glass Co., Ltd., Tokyo, Japan) to make it hydrophobic with a contact angle of ~110°. Acoustic streaming was visualized by adding red polystyrene particles (with diameters

of ~10 μm) into the water droplet. The streaming of particles was visualised using a video camera with a resolution of 720×480 pixels. Thermal effects of the droplet were recorded using an infrared (*IR*) thermal camera (FLIR T-620) with a resolution of 480×640 pixels.

For measuring streaming velocity, travel of particles have been estimated in both x and y direction using *PIV* technique with the help of the tool 'tracker'. This tool measures the distance travelled by each particle from one frame to another in both directions. Then this data had been used to calculate the velocity of particles using $U = \sqrt{(\Delta x/\Delta t)^2} + (\Delta y/\Delta t)^2$, where U is the average streaming velocity, Δx is the average change in position of particles from one frame to another in x direction. Similarly, Δy is the change in position of particles in y-direction.The velocities of particles can be different at the start of applying input power, in the middle and the end, that is why ten different time frames have been selected from the start of the *SAW* power to the end.

Mass transfer can occur either by evaporation between the droplet boundary and surroundings or by the phase change inside the droplet [28]. The following equation can predict the mass transfer (change with time),

$$\frac{dm_d}{dt} = -\dot{s}_m \qquad (1)$$

where 'm_d' is the mass of the droplet (kg), 't' the time (sec), '$\dot{s}_m$' is the source term for the mass transfer of the droplet. The source term for the mass transfer and can be further explained by $\dot{s}_m = -k_m A_t \rho_d B_m - m_d\, \dot{\chi}$, where the first term ($k_m A_t \rho_d B_m$) is the rate of droplet evaporation with 'k_m' the effective mass transfer coefficient (m/s), 'A_t' the total area of the droplet, 'ρ_d' the density of droplet liquid (kg/m^3), and 'B_m' the Spalding mass transfer number, $B_m = \frac{X_s - x_0}{1 - x_0}$, defined by droplet surface mass fraction, 'x_s', and that far away, 'x_o', respectively. The second term ($m_d\, \dot{\chi}$) is the mass transfer rate due to the phase changes, which occurs when the temperature of droplet reaches the saturation temperature, where m_d is the mass of the droplet and $\dot{\chi}$ represents the quality of the vapour. Momentum conservation is based on Newton's Second Law of Motion which can be predicted using the following equation,

$$\frac{dm_d U_d}{dt} = \sum F_i \qquad (2)$$

The forces acting on the droplet are *SAW* force, inertial force, drag force (F_d), friction force (F_r), and buoyancy force (F_b). U_d is the droplet velocity and m_d is the mass of the droplet. Based on the study [29], the *SAW* force can be predicted as,

$$F_s = -\frac{\rho_f}{\delta_x \delta_y}(1 + \alpha_1^2)^{3/2} A^2 \omega^2 k_i \int_0^{\delta_x} \int_0^{\delta_y} exp2(k_i x + \alpha_1 k_i y)\, dxdy \quad (3)$$

where 'A' is equivalent to the *SAW* wave amplitude at the edge of the liquid, $\omega = 2\pi f_0$ is the angular frequency, k_i the leaky *SAW* number (m^{-1}), 'α_1^2' is attenuation co-efficient, δ_x and δ_y are changes in the x and y direction, respectively [29]. The drag force (if droplet moves on the device surface) can be calculated by [30],

$$F_d = -0.5\, C_d A_c \rho_d U_d^2 \quad (4)$$

where A_c is the cross-sectional area of the droplet (m^2), ρ_d and U_d is the droplet density and velocity of the droplet, respectively, and C_d is the drag coefficient. Moreover, the friction force can be calculated by [30],

$$F_f = -0.5\, C_f A_f \rho_d U_x^2 + F_{f0} + F_\sigma \quad (5)$$

where A_f is the interfacial area of the drop and device (m^2), U_x is the streaming velocity inside the droplet near the substrate, F_{f0} is the static friction force and F_σ, is the interfacial tension force. F_{f0}, can be calculated using $F = N\mu$, where N is the normal force and μ is the co-efficient of friction. On the other hand, F_σ, can be predicted using $F_\sigma = \pi\sigma d$, whereas 'π' is 3.1416, 'σ' is the surface tension coefficient whose value is 27.8 mN/m for hydrophobic surface between *ZnO* and water droplet, 'd' is the diameter of the droplet (mm). Energy conservation can be estimated using the first law of thermodynamics as given,

$$\frac{dE_d}{dt} = \sum \dot{Q}_i + \dot{W} \quad (6)$$

where E_d is the total energy of the droplet (J) and $\frac{dE_d}{dt}$ is energy per unit time (J/s=W), $\dot{Q}_i$ is the rate of the *i*th heat interaction with the system, and $\dot{W}$ is the rate of mechanical interaction of the droplet with surroundings.

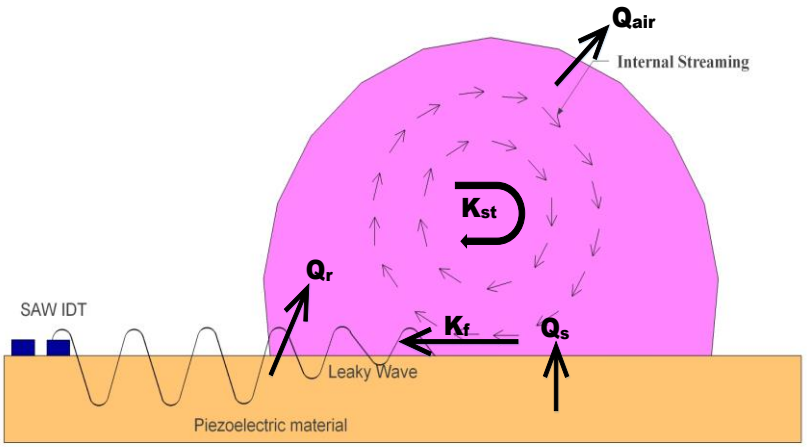

Figure 2: A thermodynamic energy conservation model of *SAW*-droplet interaction showing heat transfers and kinetic change inside the droplet.

Figure 2 shows the experimental thermodynamic analysis model of this study and has been derived using the energy conservation principle as given,

$$\dot{Q}_r + \dot{Q}_s + \dot{Q}_a = \dot{E}_d + \dot{K}_{st.} + \dot{K}_f \qquad (7)$$

$\dot{Q}_r$ is thermal impacts of the heat radiated (acousto-thermal effect) by *SAW* on both the droplet and the device substrate, as shown in Figure 2. $\dot{Q}_s$ highlights the heat transfer from the substrate surface to the droplet and $\dot{Q}_a$ is the heat transfer from the droplet to the surroundings (air). $\dot{E}_d$ (W) is the power to heat the fluid due to the increases of enthalpy, and the $\dot{K}$ (kW) mechanical (kinetic) powers whereas $\dot{K}_{st}$ is the kinetic impact of streaming and $\dot{K}_f$ is friction dissipations. The power heating the droplet can be calculated by the changes in enthalpy as,

$$\dot{E}_d = \rho_d V_d C_p \frac{dT_d}{dt} \qquad (8)$$

In this case, the change in enthalpy is the change in internal energy. $\dot{E}_d$ is the change in energy per unit time (J/s=W) whereas ρ_d is the density (kg/m^3), $V_{d,}$ the volume (m^3), C_p the heat capacity (kJ/kg K), T_d (K), the temperature of the water droplet, and $\frac{dT_d}{dt}$ is the temperature gradient. $\dot{K_{st}}$ and $\dot{K_f}$ can be predicted using equations,

$$\dot{K_{st}} = \rho_d V_d u_d \frac{du_d}{dt} \qquad (9)$$

$$\dot{K_f} = A_s \mu_d \frac{du_f}{dy} u_f \qquad (10)$$

where ρ_d (kg/m^3) is the density of the droplet, V_d (m^3) is the volume of the droplet and u_d (mm/s) is the velocity of streaming particles. $\frac{du_d}{dt}$ is the acceleration of the fluid for kinetic power in equation (9) which can be calculated by the average velocities as given,

$$\frac{du_d}{dt} = \frac{1}{3}\sum_{i=1}^{3}\frac{\left(u_i(t_2) - u_i(t_1)\right)}{\Delta t} \qquad (11)$$

where u_i is the velocity of particles at positions i=1, 2 and 3, as shown in Figure 3-b measured from the experiments.

In equation (10), A_s represents interfacial surface area, μ_d, the dynamic viscosity (N.s/m^2), $\frac{du_f}{dy}$, calculated by $\left(\frac{u_{x,x=1}-0}{\Delta y}\right)$, where u_x is the velocity component at 'x' direction close to the bottom, Δy is the thickness of bottom boundary layers and u_f (mm/s), velocity of the particles close to the substrate. Figure 3 presents the coupling of temperature distribution with the streaming inside the droplet. To obtain the precise temperature distribution, the infrared images of the droplet have been divided into 16 elements with nearly equal volume as shown in Figure 3-a. where red ovals represent the element's temperature associated to calculate $\dot{Q}_a$ and black oval represents element's temperature associated with streaming to calculate $\dot{Q}_s$. The positive (+) sign means all the elements' temperatures are added up to get the average temperature of the outer layer of the droplet.

Figure 3-b showing the droplet image for the streaming data. Position 1,2,3 represents points to predict the velocities of particles at three different positions where the velocity was measured using particles image velocimetry (*PIV*). U_1 (mm/s) is the velocity of the particles close to the substrate, U_2 (mm/s) near the top, and U_3 (mm/s) represents vortex velocities, as shown in Figure 3-b. The data from U_1 are associated with the temperature data of the black oval to be calculated $\dot{Q}_s$ and the data from U_2 are associated with the temperature data of red ovals to calculate $\dot{Q}_a$. The thermal data has been analysed by generating a code in *MATLAB* using image processing. Figure 3-c shows a processed image from *MATLAB* with a temperature of the individual element.

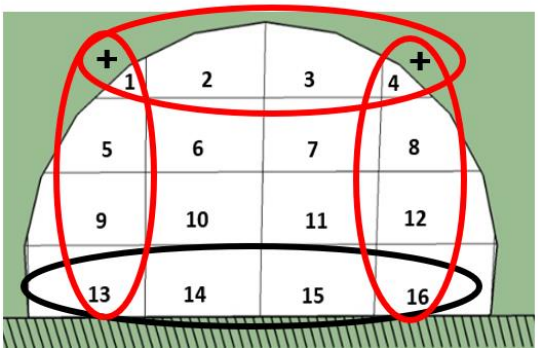

(a)

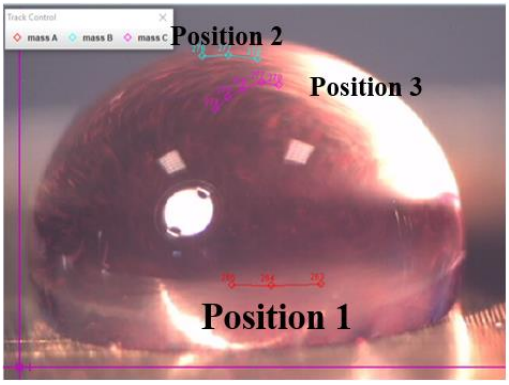

(b)

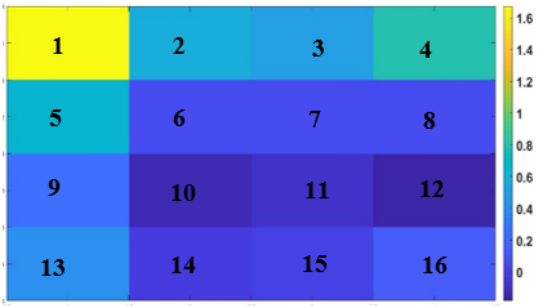

(c)

Figure 3: Coupling of kinetic and thermal impacts (a) droplet model showing 16 elements. Red and black ovals to represent the element's temperature for $\dot{Q}_a$ and $\dot{Q}_s$ respectively (b) streaming of particles at three different positions inside the droplet, (c) An image from *MATLAB* showing the temperature of 16 elements.

Different heat transfer mechanisms inside the droplet and kinetics involving friction and momentum have been calculated using different co-relations. The power due to heat transfers from the *IDT* surface to the droplet and the air from the droplet can be estimated using,

$$\dot{Q}_{\varphi} = A_{\varphi}\, \alpha_{\varphi} \left(T_{\varphi} - T_{d\varphi}\right) \qquad (12)$$

$T_{d\varphi}$ is the droplet temperature, $T\,(K)$, $\varphi = s, a$, either substrate or air, the interfacial area A (m^2). Some dimensionless numbers have been used to find the coupling between kinetics and heat transfer inside the droplet. Nusselt number, *Nu*, depicts the heat transfer of a fluid which can be related to Reynold's number, *Re*, using the formula [31],

$$Nu = \frac{\alpha_s\, L}{k} = 2 + \beta_c\, Re^{\frac{1}{2}}\, Pr^{\frac{1}{3}} \qquad (13)$$

where α_s is an effective convection heat transfer coefficient, L is the characteristic length, k is the thermal conductivity. β_c is a constant, which from experimental observation is found to be 0.6 [32].

$Re = \frac{\rho * u * L}{\mu}$, where ρ is the density of water, u is the velocity of particles inside droplet; L is the diameter of a water droplet and μ is the dynamic viscosity of the water. The value of Prandtl number, Pr, for water at room temperature is 7.56 [33]. α_s can be calculated using equation (13), and hence the heat transfers ($\dot{Q}_s$) can be found using equation (12).

Since the temperature of the droplet is higher than the surrounding air, which is stationary. Therefore, natural convection takes place near the droplet. Grashof number (Gr_L) is analogous to *Re*, represents a flow regime in natural convection, calculated using [33],

$$G_r = \frac{g\beta(T_d - T_\infty)L^3}{\nu^2} \qquad (14)$$

where g is the acceleration due to gravity, β is the coefficient of thermal expansion, $1/T_\infty$ for an ideal gas as the air. T_d is the droplet temperature, T_∞ is the air temperature, L is the diameter of the droplet, and ν is the kinematic viscosity of the air. Correlations between '*Gr*' and '*Nu*' is given,

$$Nu = \frac{\alpha_a L}{k} = 2.65(G_r\, P_r)^{1/8} \qquad (15)$$

3. Results and Discussion:

3.1: Mass and momentum conservation:

It was found from this study that no significant mass transfer takes place within the power range of this study. The droplet does not move and there is no deformation or movement of the droplet at the input power of ≤ 2.0 W. However, at an input power of 3.2 W, the droplet moves and stops within the first second of the input *SAW,* where the *SAW* force is balanced by friction and interfacial tension force.

3.2: Energy conservation:

The thermal images for the side views of the droplet taken from experiments with input power values, 0.096 W, 0.38 W, 0.96 W, 2.0 W and 3.2 W are presented in Figure 4. The *SAW* enters from the left side of the droplet for a duration of 43.0 s. A few critical time frames have been chosen to show the temperature rise of the droplet. It is pertinent to note that the thermal impact is insignificant for an input power of 0.096 W, but its impact starts at 0.38 W after 23.0 s of *SAW* acting time as shown in Figure 4-(a) and 4-(b), respectively. However, the waves' energy is not large enough to completely heat the droplet even after 43.0 s at an input power of 0.38 W.

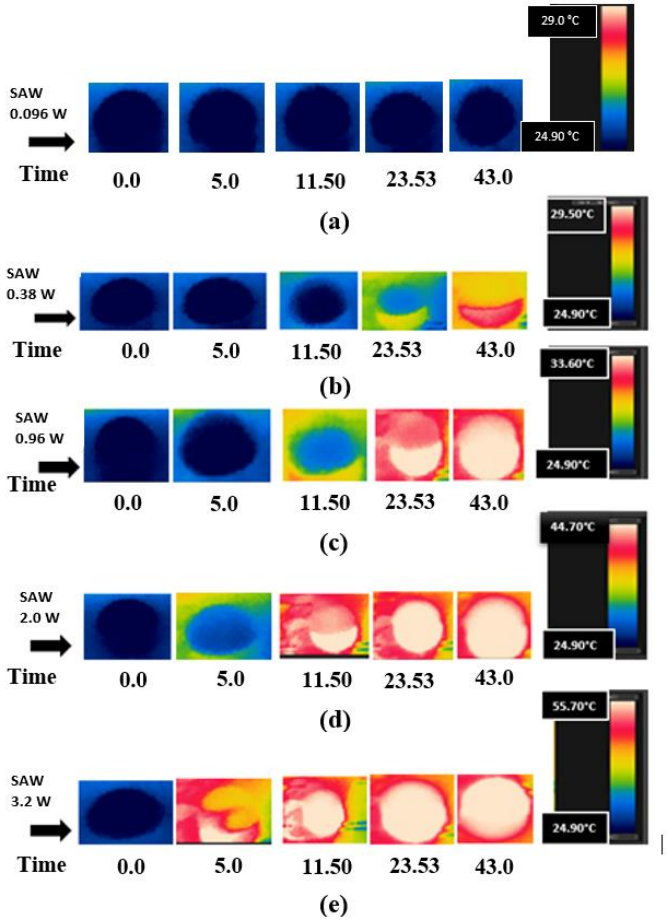

Figure 4: Thermal images of droplet at (a) 0.096 W(b) 0.38 W, (c) 0.96 W, (d) 2.0 W, (e) 3.2 W (Time 0.0, 5.0, 11.50, 23.53 and 43.0 s from left to right) observed by FLIR (T-620).

It is essential to observe that the temperature of the droplet near the substrate is more than other areas of the droplet which clearly shows that heating of the substrate plays an important role in the temperature rise of the droplet. Furthermore, impact delay is the delay time before waves start heating the droplet. It is clear from Figure 4-(b) and 4-(c) there is an impact delay of 5.0 s for input power values of 0.38 W and 0.96 W. It can be observed from Figure 4- (d) and 4-(e) that the impact delay decreases with the increase in input power.

The average temperatures of the droplet and the relation between the streaming of particles and the rise in temperature at different input power values are presented in Figure 5. The average temperature of the droplet against time is shown in Figure 5-a. The impact delay at lower input power values for critical points presented in Figure 4 has also been observed in Figure 5-a in the initial 5.0 s of the input *SAW*. For P_{in} > 0.96 W, the droplet temperature abruptly increases with time and has a larger gradient than the lower input power levels. The maximum precise T_d at input power levels of 0.096 W, 0.38 W, 0.96 W, 2.0 W, and 3.2 W is 1.02 ˚C, 4.5 ˚C, 10.05 °C, 21.92 °C, and 31.33 °C, respectively, as illustrated in Figure 5-a. The maximum rise in temperature of the droplet against the average streaming velocity of the particles (after 43.0 s of the *SAW* acting time) has been presented in Figure 5-b. Both kinetic

(streaming) and thermal impact are linearly proportional to each other, hence a correlation can be derived which has been used to find other heat transfers inside the droplet. It has to be noted that the data shown in Figure 5 is the rise (change) in temperature where the experiment was conducted at room temperature (≈ 24 °C). The initial temperature has been subtracted from the actual temperature to get the temperature rise.

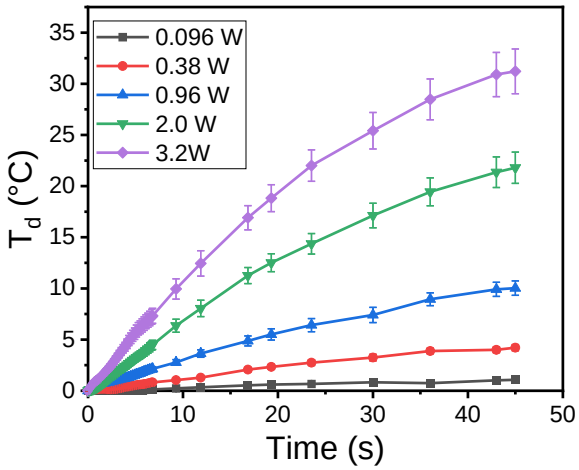

(a)

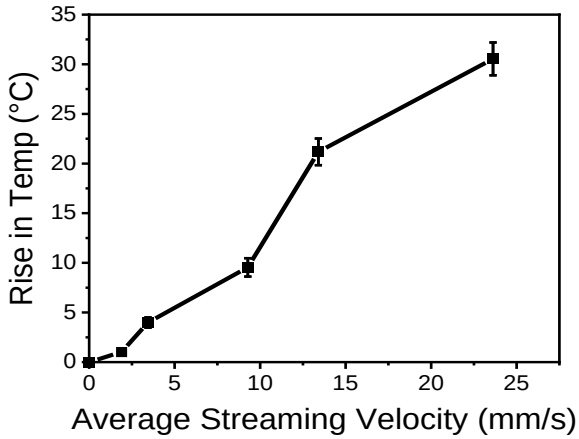

(b)

Figure 5: (a) T_d from 0.0 to 43.0 s at different power levels (0.096 W, 0.38 W, 0.96 W, 2.0 W, 3.2 W). (b) After 43.0 s of *SAW* acting time, the maximum average velocity of particles' streaming at different input power against the maximum rise in temperature of the droplet.

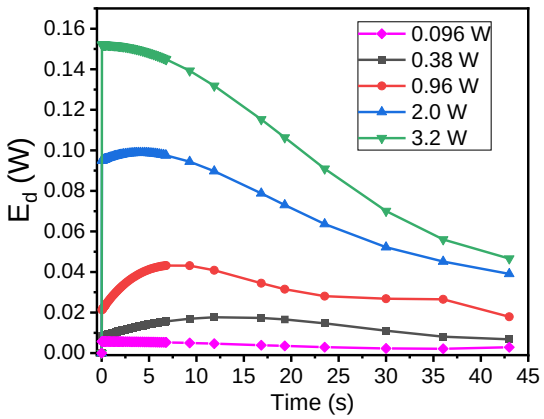

(a)

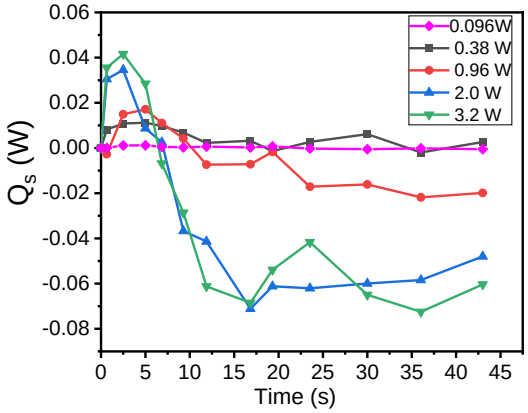

(b)

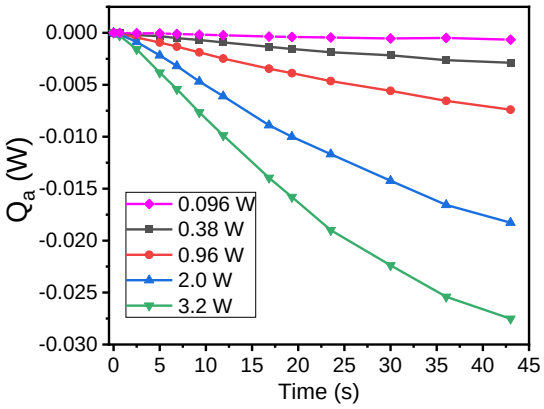

(c)

Figure 6: Rates of energy absorbed, heat transfers inside and outside of the droplet at power levels of 0.096 W, 0.38 W, 0.96 W, 2.0 W and 3.2 W (a) $\dot{E}_d$ (rate of energy absorbed by the droplet), (b) $\dot{Q}_s$ rate of heat transfer from substrate to the droplet, (c) $\dot{Q}_a$ rate of heat transfer from air to the droplet. Rates of heat transfers are measured in watts and time is measured in seconds.

Figure 6 shows rates of energy absorbed, heat transfers inside and outside of the droplet. The results show that the total energy change in enthalpy of the droplet is directly proportional to the input power, as presented in Figure 6-a. At $P_{in} \leq 0.96$ W, $\dot{E}_d$ becomes almost a constant after applying input power for 15.0 s, however, at $P_{in} > 0.96$ W, the absorbed energy continuously decreases with time. Equation

(8) reflects that $\dot{E}_d$ is proportional to the temperature gradient (dT/dt), and other values in equation (8) do not vary significantly even with the temperature change (see appendix). Therefore, $\dot{E}_d$ has a similar trend as for the temperature gradient (dT/dt) given in equation (8).

The heat transfer from the substrate to the droplet, $\dot{Q}_s$, at different input power levels for the R-waves is illustrated in Figure 6-b. At lower input power values, e.g., 0.096 W and 0.38 W, $\dot{Q}_s$ is insignificant, i.e 10^{-4} and 10^{-3} W, respectively. Moreover, at these power levels, heat is transferred from the substrate to the droplet all over time from the start to the end of *SAW* input. The heating of the droplet is caused by both heating from *SAW* radiation and the substrate.

The reverse heating transfer has also been observed. An inverse time is defined as the time after which heat transfer takes place from the droplet back to the substrate. This reverse time decreases with the increase in input power. Inverse heat transfer started at an input power of 0.96 W after 20.0 s of the *SAW* acting time as presented in Figure 6-b. Although the substrate is already heated according to the general heat transfer principle, heat always flows from higher to lower. The fluid's input power is partially absorbed and then converted into thermal power to increase the fluid's temperature, part of which is converted into kinetic energy to enhance fluid streaming. This dynamic process takes about 20.0 s in the case of 0.96 W, then the fluid on the bottom layer is heated to a temperature higher than the temperature of the substrate. Therefore, a reverse heat transfer takes place from the droplet to the substrate.

For power values of 2.0 W and 3.2 W, the droplet is heated quicker than 0.96 W, so the reverse heat transfer occurs just after five seconds of input *SAW*. However, such a small 'reverse' heat flux does not have a huge impact on the large volume of the substrate.

The sink of the heat is the heat transfer from the droplet to the air, $\dot{Q}_a$, presented in Figure 6-c. $\dot{Q}_a$ is dependent on the effective heat transfer coefficient, α_a, and the temperature difference, (T_a-T_{ds}). T_a is the temperature of the surrounding air (room temperature, 24 °C) and T_{ds} is the temperature of the outer layer of the droplet directly in contact with the air, as explained in Figure 3. A negative value of $\dot{Q}_a$ means that this is heat dissipating from the system. It is also pertinent to note that for P_{in} < 0.50 W, the magnitude of the droplet's energy received from the substrate is in the range of ~ 0.01 W to 0.02 W. However, the power lost by the droplet to the surrounding air is one order of magnitude less, e.g., ~0.002 W for the same input power as presented in Figure 6-b and c. This means the heat entered into the droplet is ten times more than the heat dissipation from the system.

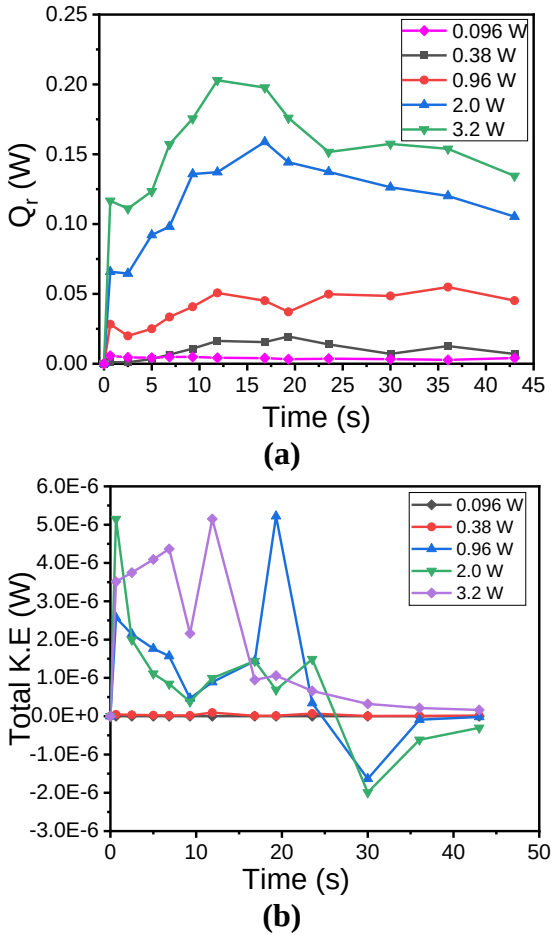

Figure 7: (a) Heat radiated inside the droplet, $\dot{Q}_r$, (b) Total K.E inside the droplet.

Radiated heat transfer, $\dot{Q}_r$, is the heat transfer caused by *SAW*, which enters from the edge of the droplet. The results of $\dot{Q}_r$ versus time are shown in Figure 7-a, and Figure 7-b shows total kinetic energy inside the droplet. At the lowest input power of 0.096 W, $\dot{Q}_r$ is insignificant (10^{-3} W), which means that there is no heat radiated inside the droplet at this P_{in}. However, at an input power of 0.38 W, the heat starts radiating after 5.0 s of the *SAW* acting time. It reaches the peak at 20.0 s and then decreases further with time. A big jump has been observed at an input power of 0.96 W at the start of *SAW* elapsed time. The same trend has been observed for 2.0 W and 3.2 W where energy transferred to the droplet is more than lower input power values, and the peak is observed after 15.0 s of *SAW* acting time. After this time, heat also starts to be transferred from the substrate to the droplet which overcomes the radiation heat transfer, and it decreases with time. The maximum value of $\dot{Q}_r$ is 0.20 W at an input power of 3.2 W.

The kinetic impact of *SAW* involves kinetic energy due to streaming inside the droplet and friction near the wall of the substrate. Kinetic energy inside the droplet drives the particles to flow and friction near the wall is one source of heat. The sum of both streaming and friction kinetic power (energy per unit time) is presented in Figure 7-b. The positive value of these kinetic means fluid absorbs power from SAW or other thermal sources whereas negative value means conversion of kinetic to thermal energy.

In Fig. 7-b), K.E is negative after 23.0 s of *SAW* input power. This is because, after this *SAW* input time, the temperature of the droplet becomes higher than the substrate and inverse heat transfer takes place. A negative value means the kinetic power is being converted to thermal energy which heats the droplet more than the substrate and becomes a mean to increase the overall temperature of the droplet. It is clear from Figure 7-b that these values are insignificant (~ 10^{-6} W) as compared to the heat transfers inside the droplet. This proves our assumption that kinetic impacts are insignificant. Negative kinetic energy means heat is dissipating from the system.

Equation (7) has been verified using the measured value. For example, at an input power of 3.2 W, after 43.0 s of *SAW* acting time, $\dot{Q}_r$ is 0.134 W, $\dot{Q}_s$ is -0.060 W, $\dot{Q}_a$ is -0.027 W. This equals to 0.046 W which is the sum of all heat transfers inside the droplet. On the other hand, at the same input power and *SAW* acting time, $\dot{E}_d$ is 0.046 W, $\dot{K}_{st.}$ is -4.18*10^{-9} W and $\dot{K}_f$ is 1.66*10^{-7} W, the sum of which is also 0.046 W. Therefore, the measured data verified energy balance within the system.

Conclusions:

Mass, momentum, and energy conservation principles have been implemented to find the coupling mechanism between kinetic and thermal impacts of *R-SAW*. Since the temperature of the droplet is in the range of 25-55 °C, there is no mass change either by evaporation or phase change. At a lower input power, the *SAW* force is balanced by frictional and interfacial tension force. However, at an input power of 3.2 W, there is a momentum that drives the droplet within less than a second, but the frictional and interfacial tension force stops the droplet. There is insignificant thermal impact at P_{in} of 0.096 W, but thermal impacts become apparent with the input power of 0.38 W and above with the impact delay. By increasing the input power further, the thermal impact starts dominating. This dominating effect can be predicted by implementing the energy conservation principle. It is concluded from this study that the streaming velocity and temperature increase are directly proportional to the input power applied. Temperature gradient (dT/dt) decreases with time as the droplet approaches the steady-state. At P_{in} < 0.50 W, heating to the droplet is mostly from the heat transferred from the substrate, which is at the same order of magnitude of the energy absorbed ($\dot{E}_d$).

The temperature of the substrate is 1.9% higher than the temperature of the bottom layer of the droplet when P_{in} < 0.50 W. However, when P_{in} > 0.50 W, the temperature of the bottom layer of the droplet becomes 2.7% more as compared to the substrate. Therefore, reverse heat transfer occurs at a higher input power, whereas reverse time occurs quicker when the input power is increased. It is concluded that heat is always transferred from the droplet to the air since the droplet's temperature is always higher than the room temperature. $\dot{Q}_r$ is highest amongst all other heat transfer mechanisms inside the droplet since this is the main cause of heat generation inside the droplet. Besides, kinetic powers (streaming and friction) are insignificant as compared to heat transfer. Furthermore, convection plays a vital role

in the droplet's temperature rise, as the portion of the droplet close to the substrate has the highest temperature and streaming in the whole droplet. The proposed model can be used to control the temperature rise of the droplet precisely by visualizing streaming, which could be applied to prevent damage to biological cells.

Acknowledgements:

We acknowledge the financial support from the UK Engineering and Physical Sciences Research Council (EPSRC) grants EP/P018998/1, and Special Interests Group of Acoustofluidics under the EPSRC-funded UK Fluidic Network (EP/N032861/1). The authors are thankful to the University of Northumbria Newcastle upon Tyne for providing the experimental setup for this work. The authors are thankful to Heriot-Watt University for their support.

Conflict of Interest:

There are no conflicts to declare.

Authors Contribution:

Mubbashar Mehmood: Conceptualization, data curation, investigation, methodology, writing original draft, review and editing. Tariq Nawaz Chaudhary: Validation, visualization, writing-reviewing and editing. Umar F khan: Software, validation, visualization, writing- original draft, review and editing. Stephen Burnside: Visualization, writing- review and editing. Baixin Chen and Richard Fu: Conceptualization, supervision, funding acquisition, validation, writing -original draft, review and editing.

References:

[1] J. Kondoh, N. Shimizu, Y. Matsui, M. Sugimoto, and S. Shiokawa, "Development of SAW thermocycler for small liquid droplets," in *IEEE Ultrasonics Symposium, 2005.*, 2005, vol. 2, pp. 1023–1027.

[2] A. Wixforth, "Acoustically driven planar microfluidics," *Superlattices Microstruct.*, vol. 33, no. 5, pp. 389–396, 2003.

[3] C. Chen *et al.*, "Three-dimensional numerical simulation and experimental investigation of boundary-driven streaming in surface acoustic wave microfluidics," *Lab Chip*, vol. 18, no. 23, pp. 3645–3654, 2018.

[4] H. Zec, D. J. Shin, and T.-H. Wang, “Novel droplet platforms for the detection of disease biomarkers,” *Expert Rev. Mol. Diagn.*, vol. 14, no. 7, pp. 787–801, 2014.

[5] A. Wixforth, C. Strobl, C. Gauer, A. Toegl, J. Scriba, and Z. v Guttenberg, “Acoustic manipulation of small droplets,” *Anal. Bioanal. Chem.*, vol. 379, no. 7–8, pp. 982–991, 2004.

[6] J. Kondoh, N. Shimizu, Y. Matsui, M. Sugimoto, and S. Shiokawa, “Development of temperature-control system for liquid droplet using surface Acoustic wave devices,” *Sensors Actuators A Phys.*, vol. 149, no. 2, pp. 292–297, 2009.

[7] S. Li, J. Desrosiers, and V. R. Bhethanabotla, “Heating of Rayleigh surface acoustic wave devices in 128° YX LiNbO 3 and ST X quartz substrates,” in *2017 IEEE SENSORS*, 2017, pp. 1–3.

[8] H. Sakamoto *et al.*, “Electrochemical characteristics of a hyperthermophilic enzyme in microdroplets stirred and heated by surface acoustic waves,” *Biotechnol. Prog.*, vol. 36, no. 2, p. e2943, 2020.

[9] M. Alghane, Y. Q. Fu, B. X. Chen, Y. Li, M. P. Y. Desmulliez, and A. J. Walton, “Streaming phenomenon in microdroplets induced by Rayleigh surface acoustic wave,” *Microfluid. Nanofluidics*, vol. 13, no. 6, pp. 919–927, 2012.

[10] A. N. Darinskii, M. Weihnacht, and H. Schmidt, “Surface acoustic wave electric field effect on acoustic streaming: Numerical analysis,” *J. Appl. Phys.*, vol. 123, no. 1, p. 14902, 2018.

[11] T. Zheng, C. Wang, Q. Hu, and S. Wei, “The role of electric field in microfluidic heating induced by standing surface acoustic waves,” *Appl. Phys. Lett.*, vol. 112, no. 23, p. 233702, 2018.

[12] S. Ito, M. Sugimoto, Y. Matsui, and J. Kondoh, “Study of surface acoustic wave streaming phenomenon based on temperature measurement and observation of streaming in liquids,” *Jpn. J. Appl. Phys.*, vol. 46, no. 7S, p. 4718, 2007.

[13] Z. J. Jiao, X. Y. Huang, and N.-T. Nguyen, “Scattering and attenuation of surface acoustic waves in droplet actuation,” *J. Phys. A Math. Theor.*, vol. 41, no. 35, p. 355502, 2008.

[14] J. Yang and Y. Yang, “Metal–organic frameworks for biomedical applications,” *Small*, vol. 16, no. 10, p. 1906846, 2020.

[15] H. Furukawa, K. E. Cordova, M. O’Keeffe, and O. M. Yaghi, “The chemistry and applications of metal-organic frameworks,” *Science (80-.).*, vol. 341, no. 6149, 2013.

[16] C. Xu, T. Zheng, Y. Liu, and C. Wang, “Acoustomicrofluidic synthesis of hierarchically porous metal-organic frameworks,” *Mater. Lett.*, vol. 285, p. 129052, 2021.

[17] P. J. Hung, P. J. Lee, P. Sabounchi, R. Lin, and L. P. Lee, “Continuous perfusion microfluidic cell culture array for high-throughput cell-based assays,” *Biotechnol. Bioeng.*, vol. 89, no. 1, pp. 1–8, 2005.

[18] V. Miralles, A. Huerre, F. Malloggi, and M.-C. Jullien, “A review of heating and temperature control in microfluidic systems: techniques and applications,” *Diagnostics*, vol. 3, no. 1, pp. 33–67, 2013.

[19] R. J. Shilton *et al.*, “Rapid and controllable digital microfluidic heating by surface acoustic waves,” *Adv. Funct. Mater.*, vol. 25, no. 37, pp. 5895–5901, 2015.

[20] Y. Wang *et al.*, “A rapid and controllable acoustothermal microheater using thin film surface acoustic waves,” *Sensors Actuators A Phys.*, vol. 318, p. 112508, 2021.

[21] Y. Wang *et al.*, "Acoustofluidics along inclined surfaces based on AlN/Si Rayleigh surface acoustic waves," *Sensors Actuators, A Phys.*, vol. 306, 2020.

[22] Q.-Y. Huang, Q. Sun, H. Hu, J.-L. Han, and Y.-L. Lei, "Thermal effect in the process of surface acoustic wave atomization," *Exp. Therm. Fluid Sci.*, vol. 120, p. 110257, 2021.

[23] J. Zhou *et al.*, "Nebulization using ZnO/Si surface acoustic wave devices with focused interdigitated transducers," *Surf. Coatings Technol.*, vol. 367, pp. 127–134, 2019.

[24] D. Beyssen, F. Sarry, and T. Roux-Marchand, "Correlation of heat transfers mechanism (s) and time constant equilibrium on digital Rayleigh-SAW microfluidic system," *Procedia Eng.*, vol. 120, pp. 1067–1070, 2015.

[25] Y. Q. Fu *et al.*, "Recent developments on ZnO films for acoustic wave based bio-sensing and microfluidic applications: a review," *Sensors Actuators B Chem.*, vol. 143, no. 2, pp. 606–619, 2010.

[26] X. Y. Du *et al.*, "ZnO film thickness effect on surface acoustic wave modes and acoustic streaming," *Appl. Phys. Lett.*, vol. 93, no. 9, p. 94105, 2008.

[27] Y. Q. Fu *et al.*, "Advances in piezoelectric thin films for acoustic biosensors, acoustofluidics and lab-on-chip applications," *Prog. Mater. Sci.*, 2017.

[28] V. K. Dhir, "Boiling heat transfer," *Annu. Rev. Fluid Mech.*, vol. 30, no. 1, pp. 365–401, 1998.

[29] M. M. Alghane, "Surface acoustic wave streaming in a microfluidic system." Heriot-Watt University, 2013.

[30] F. M. White, *Fluid mechanics*. McGraw-hill, 1999.

[31] S. S. Sazhin, “Advanced models of fuel droplet heating and evaporation,” *Prog. Energy Combust. Sci.*, vol. 32, no. 2, pp. 162–214, 2006.

[32] R. B. Bird, W. E. Stewart, and E. N. Lightfoot, *Transport phenomena*. John Wiley & Sons, 2007.

[33] Y. Cengel, *Heat and mass transfer: fundamentals and applications*. McGraw-Hill Higher Education, 2014.